

Quasi-two-dimensional heterostructures (KM_{1-x}Te)(LaTe_3) ($M = \text{Mn, Zn}$) with charge density waves

Jin-Ke Bao^{1,2}, Christos D. Malliakas³, Chi Zhang⁴, Songting Cai⁴, Haijie Chen^{1,3}, Alexander J. E. Rettie⁵, Brandon L. Fisher⁶, Duck Young Chung¹, Vinayak P. Dravid⁴, and Mercuri G. Kanatzidis^{1,3,*}

¹Materials Science Division, Argonne National Laboratory, Lemont, Illinois 60439, United States,

²Laboratory of Crystallography, University of Bayreuth, 95447 Bayreuth, Germany

³Department of Chemistry, Northwestern University, Evanston, Illinois 60208, United States,

⁴Department of Materials Science and Engineering, Northwestern University, Evanston, Illinois 60208, United States,

⁵Electrochemical Innovation Lab, Department of Chemical Engineering, University College London, London WC1E 7JE, United Kingdom,

⁶Center for Nanoscale Materials, Nanoscience and Technology Division, Argonne National Laboratory, Lemont, Illinois, 60439, United States.

Abstract

Layered heterostructure materials with two different functional building blocks can teach us about emergent physical properties and phenomena arising from interactions between the layers. We report the intergrowth compounds $\text{KLaM}_{1-x}\text{Te}_4$ ($M = \text{Mn, Zn}$; $x \approx 0.35$) featuring two chemically distinct alternating layers $[\text{LaTe}_3]$ and $[\text{KM}_{1-x}\text{Te}]$. Their crystal structures are incommensurate, determined by single X-ray diffraction for the Mn compound and transmission electron microscope (TEM) study for the Zn compound. $\text{KLaMn}_{1-x}\text{Te}_4$ crystallizes in the orthorhombic superspace group $Pnmm(01/2\gamma)s00$ with lattice parameters $a = 4.4815(3)$ Å, $b = 21.6649(16)$ Å and $c = 4.5220(3)$ Å. It exhibits charge density wave (CDW) order at room temperature with a modulation wave vector $\mathbf{q} = 1/2\mathbf{b}^* + 0.3478\mathbf{c}^*$ originating from electronic instability of Te-square nets in $[\text{LaTe}_3]$ layers. The Mn analog exhibits a cluster spin glass behavior with spin freezing temperature $T_f \approx 5$ K attributed to disordered Mn vacancies and competing magnetic interactions in the $[\text{Mn}_{1-x}\text{Te}]$ layers. The Zn analog also has charge density wave order at room temperature

with a similar \mathbf{q} -vector having the \mathbf{c}^* component ~ 0.346 confirmed by selected-area electron diffraction (SAED). Electron transfer from $[KM_{1-x}Te]$ to $[LaTe_3]$ layers exists in $KLaM_{1-x}Te_4$, leading to an enhanced electronic specific heat coefficient. The resistivities of $KLaM_{1-x}Te_4$ ($M = Mn, Zn$) exhibit metallic behavior at high temperatures and an upturn at low temperatures, suggesting partial localization of carriers in the $[LaTe_3]$ layers with some degree of disorder associated with the M atom vacancies in the $[M_{1-x}Te]$ layers.

Introduction

Hetero-layered structures, consisting of two or more chemically different types of layers stacked in an alternating sequence, can exhibit emergent physical properties. For example, the discovery of cuprate¹ and Fe-based² high- T_c superconductors containing $[\text{CuO}_2]^{2-}$ and $[\text{FeAs}]^-$ layers, respectively, have been in fact hetero-layered structures. Such materials harbor special states such as charge density waves (CDW) or spin density waves (SDW) which can be manipulated via external chemical or physical stimuli.³⁻⁴ It is natural to wonder what properties may appear when combining distinct functional layers in a single compound and how they may couple to one another. Hetero-layered structures can provide a versatile testbed to explore antagonistic interactions such as between superconductivity and magnetism that may be present in different layers, exemplified by the novel magnetic superconductor $\text{RbEuFe}_4\text{As}_4$ with both superconducting $[\text{FeAs}]^-$ layers and ferromagnetic Eu layers.⁵⁻⁶ In addition, the $\text{Sr}_2M'_3\text{As}_2\text{O}_2$ ($M' = \text{Cr}, \text{Mn}$) present a typical example to successfully intergrow $[M'\text{O}_2]^{2-}$ and $[M'\text{As}]^-$ along c axis with Sr^{2+} ions acting as a separating layer to connect the stacked $[M'\text{O}_2]^{2-}$ and $[M'\text{As}]^-$ layers and balance the charge in those compounds.⁷⁻⁸ They exhibit complicated magnetism and magnetic interaction between $[M'\text{O}_2]^{2-}$ and $[M'\text{As}]^-$ layers.⁷⁻⁸ A distinct type in this class are the so-called misfit layer compounds $([\text{RQ}]_{1+\delta})_m(M''\text{Q}_2)_n$ ($R = \text{Pb}, \text{Sn}, \text{Bi}$, rare earth elements; $M'' = \text{Ti}, \text{V}, \text{Cr}, \text{Nb}, \text{Ta}$; $Q = \text{S}, \text{Se}$),⁹⁻¹⁰ where each repeat unit consists of m layers of rock-salt $[\text{RQ}]$ and n layers of transition metal dichalcogenide $[M''\text{Q}_2]$ blocks. This stacking forms an incommensurate modulated heterostructure due to the mismatch of the lattice parameter from two sublattices along one axis. Since electron transfer between different functional layers can happen because of the different chemical potentials,¹¹⁻¹² we can expect a large breadth of chemical characteristics, structure types and band structures from the hetero-layered family of solids.

Most hetero-layered structures have been discovered by accident given that a substantial knowledge gap exists on how to reliably synthesize such structures. There are a number of strategies one can envision about creating hetero-layered structures.¹³⁻¹⁴ Here we show a direct synthesis approach by solid state reactions of appropriate precursors. One important question is what are the defining chemical characteristics and structural attributes that must be present in the reaction or selection of building blocks for a successful synthesis. How much can the two layered sublattices differ before the hetero-layered compounds can be destabilized? What is the role of “chemical compatibility” between the two slabs to favor the hetero-layered motif, as opposed to a phase separate mixture of homo-layered or other phases? To address such questions will require development of suitable synthesis science for hetero-layered structures and the results reported here are a contribution in this direction.

Following the general idea of creating new functional heterostructures, see Figure 1, we tried intergrowing a functional building block Te-square nets hosting a CDW order¹⁵ and anti-PbO-type building blocks.⁴ Our synthesis yielded two Q2D heterostructures $\text{KLaM}_{1-x}\text{Te}_4$ ($M = \text{Mn}, \text{Zn}$) with intact intergrown $[\text{LaTe}_3]$ and $[\text{KM}_{1-x}\text{Te}]$ layers. Single crystal X-ray diffraction analysis, transmission electron microscopy (TEM), coupled with physical property measurements including magnetic susceptibility, charge transport and heat capacity indicate that these are CDW compounds with substantial electron transfer from $[\text{KM}_{1-x}\text{Te}]$ to $[\text{LaTe}_3]$ layers. The Mn analog features massive Mn vacancies that give rise to cluster spin glass (SG) behavior with a spin freezing temperature $T_f \approx 5$ K.

Experimental Section

Synthesis. Potassium metal pieces (99.5%, Sigma), lanthanum powder and pieces (99.7%, Alfa Aesar), manganese powder (99.95%, Alfa Aesar), zinc powder (99.9%, Alfa Aesar) and tellurium chunks (99.999%, Plasmaterials) were used as the reagents for the synthesis as received. The lanthanum powder was sealed in an ampoule under argon when it was delivered and the ampoule was opened inside the glovebox. All the reactions were performed in evacuated fused-silica ampoules (I.D. = 13 mm) under a vacuum of $\sim 3 \times 10^{-3}$ mbar. We prepared two binary precursors, LaTe_3 and K_2Te_3 for synthesis of $\text{KLaM}_{1-x}\text{Te}_4$. La and Te chunks were used to prepare the precursor LaTe_3 . Fine La powder should be avoided in this reaction due to the violent exothermic reaction. Typically, 0.47 g (3.4 mmol) La pieces and 1.31 g (10.2 mmol) Te pieces were loaded into the ampoules, which were heated up to 1073 K in 24 h and held at this temperature for 24 h. LaTe_3 was ground into fine powder before it was used for further reactions. K_2Te_3 was synthesized by reacting K and Te pieces in a stoichiometric composition. 0.31 g (8 mmol) of K pieces were put on the top of 1.53 g (12 mmol) of Te pieces in a fused-silica ampule. The mixture was slowly heated to 393 K in 20 h and held for 12 h before it cooled down to room temperature. Splashes of K metals were often observed from the violent reaction of K metal with Te pieces. The reaction was then rapidly heated to 723 K in 3 h and held for 2 h before the furnace was shut off. A single black ingot of K_2Te_3 was easily removed from the ampule. The obtained K_2Te_3 was ground and used for $\text{KLaMn}_{1-x}\text{Te}_4$ crystal growth.¹⁶⁻¹⁷

K_2Te_3 , Mn or Zn powder, Te pieces and La powder were mixed in a composition “ $\text{K}_8\text{LaMn}(\text{Zn})_{0.65}\text{Te}_{20}$ ”, which were loaded into a fused-silica ampule. The mixture was heated to 973 K with a rate of 15 K h^{-1} , held for 24 h and then cooled down to 573 K at a rate of 2 K h^{-1} . The KTe_y flux was then removed using *N,N*-Dimethylformamide under N_2 gas flow to obtain shiny brown square-plate crystals, see the insets of Figure 2. Polycrystalline $\text{KLaMn}_{1-x}\text{Te}_4$ (total mass $\sim 1 \text{ g}$) was

synthesized by directly loading Te pieces, LaTe_3 , Mn powder and K pieces into a fused-silica ampule before being flame-sealed under vacuum in an appropriate composition. The mixture was slowly heated to 673 K in 20 h and held for 24 h. The pre-reacted mixture was ground in an agate mortar and heated to 773 K for another 48 h. Finally, the $\text{KLaMn}_{1-x}\text{Te}_4$ powder was ground again, pressed into a pellet and annealed at 623 K for another 48 h. This procedure gave the best phase-pure $\text{KLaMn}_{0.65}\text{Te}_4$ product judged by powder X-ray diffraction (PXRD) patterns, see Figure S1 in supporting information (SI). Polycrystalline sample $\text{KLaZn}_{1-x}\text{Te}_4$ was synthesized using the same procedure under the slightly different stoichiometry $\text{KLaZn}_{0.67}\text{Te}_4$ to get the purest phase. $\text{KLaM}_{1-x}\text{Te}_4$ ($M = \text{Mn}, \text{Zn}$) are thermodynamically stable phases. The formation of these phases does not closely depend on the initial starting materials as long as the composition is close to $\text{KLaM}_{1-x}\text{Te}_4$. The synthetic methods described here lead to samples in the best quality.

Powder X-ray Diffraction. PXRD were performed by a PANalytical diffractometer X'Pert with a Cu K_α radiation. $\text{KLaM}_{1-x}\text{Te}_4$ ($M = \text{Mn}, \text{Zn}$) samples are slightly air-sensitive and deteriorate into other phases such as Te element when exposed in air for a long time, see the case of Zn compound in Figure S2 in SI. Thus a thin Kapton film was covered on the plate sample holder to protect samples from being exposed to air. $\text{KLaMn}_{1-x}\text{Te}_4$ and $\text{KLaZn}_{1-x}\text{Te}_4$ have the same PXRD pattern with only a slight shift in the diffraction angle, indicating they have the same average crystal structure with different lattice parameters. Plate-like crystals were oriented on the sample stage to observe only $(0k0)$, see Figure 2. The lattice parameter b was extracted by least squares fitting of selected high-intensity Bragg peaks after introducing a zero-shift parameter.

Single X-ray Diffraction. Single crystal diffraction data of $\text{KLaMn}_{1-x}\text{Te}_4$ were collected on the diffractometer STOE IPDS 2T equipped with a 34-cm image plate detector at 293 K. Since $\text{KLaMn}_{1-x}\text{Te}_4$ crystals are air-sensitive, crystals were sealed in glass capillaries before the single

X-ray diffraction measurements. Basic lattice parameters and the modulation vector were extracted from the instructed reciprocal space from all the measured frames by X-area software package.¹⁸ Data reduction of main Bragg and satellites reflections and absorption correction were also done by the X-area package. The modulated structure of $\text{KLaMn}_{1-x}\text{Te}_4$ was solved and refined by the JANA2006¹⁹ software using the (3+1)-dimensional superspace method. Two modulation waves consisting of positional displacement and thermal atomic displacement parameters (ADP) were applied to each atom. The basic refinement results are summarized in Table 1 in the main text. Detailed structure information including atomic positions in each unit cell, anisotropic displacements, two modulation waves, bond lengths can be found in Table S1-5 in SI. The crystals of $\text{KLaZn}_{1-x}\text{Te}_4$ were very soft and malleable which makes it hard to obtain good single crystal diffraction data for structural refinements. The dense dislocation defects observed by TEM in the $\text{KLaZn}_{1-x}\text{Te}_4$ may also be attributed to this crystal behavior, see Figure S7 in SI.

Specific Heat. Specific heat measurements were done on the commercial Physical Property Measurement System (DynaCool, Quantum Design) using a thermal relaxation method. A tiny amount of N grease was applied to the heat capacity puck and the addenda data of the puck and N grease was collected first. Polycrystalline samples $\text{KLaMn}_{1-x}\text{Te}_4$ or $\text{KLaZn}_{1-x}\text{Te}_4$ were then cut and polished into a suitable dimension ($\sim 2 \times 2 \times 0.3 \text{ mm}^3$) for specific heat measurements. Two measurements of specific heat in the same batch were done for both $\text{KLaMn}_{1-x}\text{Te}_4$ and $\text{KLaZn}_{1-x}\text{Te}_4$. The two data sets are almost same below 100 K for both compounds while they have a small difference at high temperature especially for the case of $\text{KLaZn}_{1-x}\text{Te}_4$. This is probably due to N grease or impurity phases of which the influences to the two separately prepared samples are slightly different, see Figure S4 in SI. The data below 60 K with no influence from those two possible factors are presented and analyzed in the main text.

Magnetic Susceptibility. DC magnetic susceptibility measurements were performed on the commercial Magnetic Property Measurement System (MPMS3, Quantum Design) in a vibrating sample magnetometer mode. Lots of $\text{KLaMn}_{1-x}\text{Te}_4$ single crystals were carefully selected from the same batch. They were mounted on the quartz sample holder by N grease, where the crystals (~ 3 mg) were oriented and a magnetic field was applied parallel to ac plane. A small piece of $\text{KLaMn}_{1-x}\text{Te}_4$ or $\text{KLaZn}_{1-x}\text{Te}_4$ cut from a polycrystalline pellet was mounted on a brass holder for magnetic property measurements. Zero field cooling (ZFC) and field cooling (FC) procedures were done to check any magnetic hysteresis in the sample. Single crystals and polycrystalline pellets of $\text{KLaMn}_{1-x}\text{Te}_4$ gave similar temperature-dependent magnetic susceptibilities with exactly the same temperature of the cusp T_f under ZFC procedures. AC magnetic susceptibility measurements were carried out on the Physical Property Measurement System with frequencies in the range from 11 to 9995 Hz. Several pieces of polycrystalline ingots (~ 500 mg) were loaded into a liquid sample holder and an AC driving field of 10 Oe was applied. The freezing temperature T_f at each frequency was extracted by fitting the peak curve with a polynomial function and then finding the local maximum near the cusp position.

Results and Discussion

New Hetero-layered Compound Exploration. Following the basic idea of intergrowth of two functional layers, see Figure 1, we initially targeted hetero-layered compounds such as those combining $[\text{LaTe}_3]$ (CDW layer) and $[\text{KFeAs}]$ (high- T_c superconducting layer). These attempts were unsuccessful presumably because of significant in-plane lattice mismatch between LaTe_3 ($a \approx 4.3\text{-}4.4 \text{ \AA}$)¹⁵ and $A\text{FeAs}$ ($A = \text{K, Na}$) ($a \approx 3.9\text{-}3.95 \text{ \AA}$).²¹ We then tried KMnAs (magnetic layer) with an in-plane lattice parameter ($a \approx 4.39 \text{ \AA}$)²² close to that of LaTe_3 , however, no intergrown

products could be detected by PXRD suggesting that transition metal arsenide layers may be incompatible with Te-square lattices. KMnAs was transformed into a ternary compound telluride KMnTe_2 when it reacted with LaTe_3 at high temperatures. A switch to transition metal tellurides was then adopted which led to two hetero-layered compounds $\text{KLaM}_{1-x}\text{Te}_4$ ($M = \text{Zn, Mn}$) with Te-square nets and $[\text{M}_{1-x}\text{Te}]$ layers. We also tried other transition metals (Fe, Co, Ni, Ru, Rh, Pd, Re, Ir, Pt) to replace Mn or Zn. None of them could form this intergrowth structure. The reason may be the lack of stable $[\text{T}_{1-x}\text{Te}]$ ($T = \text{transition metal}$) blocks with these metals or significant in-plane lattice mismatch between $[\text{KFe}_{1-x}\text{Te}]$ ($[\text{FeTe}]$ blocks, $a \approx 3.8 \text{ \AA}$)²³ and $[\text{LaTe}_3]$ ($a \approx 4.3\text{-}4.4 \text{ \AA}$).¹⁵ As shown in Figure 1, two functional layers can carry electric charges, which are charge-balanced and bonded together by extra layers between them. As a result, in-plane lattice parameter match plays an important role in stabilizing this kind of intergrowth structure as discussed below.¹⁴ However, in-plane lattice parameter match is not a requisite for many misfit layer compounds where the in-plane lattice parameters from two the different layers along do not completely match.⁹ The lattice mismatch drives them to form an incommensurate modulated structure along one axis while they share the same periodicity along the other two axes. Two favorable factors stabilize such misfit layer structures: a) Strong intralayer but weak interlayer bonding; b) charge transfer between those two layers which acts an essential glue to stick them together by the attractive Coulomb interaction from oppositely charged layers.²⁴⁻²⁷ Charge transfer from $[\text{KM}_{1-x}\text{Te}]$ to $[\text{LaTe}_3]$ in $\text{KLaM}_{1-x}\text{Te}_4$, which will be proved below, likely helps stabilize the intergrowth structure.

Crystal Structure. The basic crystal structure of $\text{KLaMn}_{1-x}\text{Te}_4$ can be interpreted as the intergrowth of alternating $[\text{LaTe}_3]$ ¹⁵ and $[\text{KMn}_{1-x}\text{Te}]$ ²⁸ layers, see Figure 3. Each $[\text{LaTe}_3]$ layer consists of a buckled rock-salt $[\text{LaTe}]$ layer sandwiched by two distorted Te-square nets. The $[\text{KMn}_{1-x}\text{Te}]$ layers are composed of anti-PbO-type $[\text{Mn}_{1-x}\text{Te}]$ layers (with Mn vacancies) and

charge balancing K ions. When x is 0.5, the layers become identical to those in KMnTe_2 .²⁸ In the $[\text{Mn}_{1-x}\text{Te}]$ layers, the MnTe_4 tetrahedra are connected to each other by sharing edges and corners while they only share corners in KMnTe_2 ($x = 0.5$).²⁸ The average structure of $\text{KLaMn}_{1-x}\text{Te}_4$ at room temperature was solved and refined from single crystal X-ray diffraction data in the orthorhombic space group $Pmnm$ with lattice parameters $a = 4.4815(3)$ Å, $b = 21.6649(16)$ Å and $c = 4.5220(3)$ Å. The b parameter is the stacking axis and directed perpendicular to the crystal plate, Figure 2(a). The $\text{KLaZn}_{1-x}\text{Te}_4$ is isostructural with a smaller b lattice parameter (21.46 Å), see Figure 2(b). The corresponding parameter in $\text{KLaMn}_{1-x}\text{Te}_4$ is very close to the summation of the thickness of $[\text{LaTe}_3]$ ($b/2 = 13.113$ Å) and $[\text{KMn}_{0.5}\text{Te}]$ ($c/2 = 7.454$ Å) layers, providing a straightforward criterion to check the success of the intergrowth during the exploration using PXRD data. The in-plane lattice parameters in LaTe_3 ($a = 4.3944$ Å, $c = 4.4076$ Å)¹⁵ are comparable to KMnTe_2 ($a = b = 4.5110$),²⁸ which is important to stabilize the heterostructure $\text{KLaMn}_{1-x}\text{Te}_4$ as exemplified in many intergrowth compounds.²⁹⁻³⁰ The average distance between K and Te within $[\text{KMn}_{1-x}\text{Te}]$ layers is around 3.6 Å, only slightly smaller than the value (3.7 Å) between $[\text{KMn}_{1-x}\text{Te}]$ and $[\text{LaTe}_3]$ layers, indicating a significant interlayer bonding. The average bond length between Mn and Te in the $[\text{Mn}_{1-x}\text{Te}]$ layer is 2.772 Å, which is slightly larger (2.757 Å) than that observed in the $[\text{Mn}_{0.5}\text{Te}]$ layer of another hetero-layered compound $\text{BaFMn}_{0.5}\text{Te}$.²⁰ Although the value of Mn vacancy is close to a rational number 1/3, the diffraction data don't support the scenario of Mn-vacancy ordering in the $[\text{Mn}_{1-x}\text{Te}]$ layer. The spin-glass behavior at low temperature shown below in $\text{KLaMn}_{1-x}\text{Te}_4$ is also consistent with the disordered model of Mn vacancies in the $[\text{Mn}_{1-x}\text{Te}]$ layer, different from the case in $\text{BaFMn}_{0.5}\text{Te}$ which enters an antiferromagnetic ground state because of the Mn vacancy ordering in the $[\text{Mn}_{0.5}\text{Te}]$ layer.²⁰ The refined Mn vacancy from a disordered model is $x \approx 0.35$ which is close to both the composition

used in synthesis of $\text{KLaMn}_{1-x}\text{Te}_4$ and the composition determined by EDS in SI. This agreement on the x in the compositions above also applies to the Zn case. Since the actual value of Mn or Zn vacancies does not influence the conclusions, for convenience the composition $\text{KLaM}_{1-x}\text{Te}_4$ ($M = \text{Mn, Zn}$) with $x \approx 0.35$ is adopted in the whole article, emphasizing that massive vacancies exist in these compounds.

The square-Te nets in $\text{KLaMn}_{1-x}\text{Te}_4$ are introduced by the $[\text{LaTe}_3]$ layers whose CDW order has been well confirmed and studied in the RETe_3 ($\text{RE} = \text{rare earth elements}$) compounds.^{15, 31-32} As expected, $\text{KLaMn}_{1-x}\text{Te}_4$ also exhibits CDW order originating from the same square-Te nets at room temperature. The actual transition temperature can be very high, which is not determined in this study and needs to be further investigated by high-temperature physical property measurements. This CDW order imposes an orthorhombic distortion of the ac plane in $\text{KLaMn}_{1-x}\text{Te}_4$, which gives an incommensurate modulation wave vector $\mathbf{q} = 1/2\mathbf{b}^* + 0.3478\mathbf{c}^*$. This \mathbf{q} -vector is similar to $1/2\mathbf{b}^* + 0.3861\mathbf{c}^*$ in KLaCuTe_4 having a CDW order above room temperature but it is significantly different from the value $0.2751\mathbf{c}^*$ in LaTe_3 .^{15, 17} The magnitude of \mathbf{q} -vector in the square-Te nets is strongly dependent on the electronic filling in the CDW. Assuming the \mathbf{q} -vector in the homolayered LaTe_3 represents a baseline where no electronic transfer exists from another layer, the interlayer coupling between two different layers of $\text{KLaMn}_{1-x}\text{Te}$ in the form of electron transfer between the heterolayers can be assessed by the different \mathbf{q} -vector.

The modulated structure of $\text{KLaMn}_{1-x}\text{Te}_4$ adopts the superspace group $Pmnm(01/2\gamma)s00$, see Table 1. The atomic displacement amplitudes of the modulated waves in Te-square nets (Te(2) and Te(3) atoms) are much larger than other atoms, see Table S3 in SI, proving that CDW order is originating from the electronic instability of those nets. The CDW in the Te-square nets in $\text{KLaMn}_{1-x}\text{Te}_4$ causes distortions from the ideal square-net motif with Te(2)-Te(3) distances ranging from 2.940(7) to

3.360(7) Å, see lower panel of Figure 4. The distorted Te-square nets mainly consist of Te trimers separated by monomers and dimers with a Te-Te distance threshold of 3.08 Å, see the upper panel of Figure 4. The distribution of those Te fragments in $\text{KLaMn}_{1-x}\text{Te}_4$ is different from KLaCuTe_4 ¹² and LaTe_3 ¹⁵, suggesting different degrees of electronic density on the [LaTe₃] layer. Although the detailed modulation structure of $\text{KLaZn}_{1-x}\text{Te}_4$ has not been resolved, it is likely similar to the Mn analog as shown in the SAED pattern below. The formula can be written as $[\text{K}^+\text{M}^{2+}_{1-x}\text{Te}^{2-}]^{1-2x}[\text{Te}^{2-}_{2-2x-2}\text{La}^{3+}\text{Te}^{2-}]^{2x-1}$ ($x \approx 0.35$). This scenario is also supported by an enhanced electronic specific heat coefficient γ compared to the compound LaTe_3 shown below.

$\text{KLaZn}_{1-x}\text{Te}_4$ adopts the same average structure as $\text{KLaMn}_{1-x}\text{Te}_4$, which is supported by the PXRD patterns, see Figure S1. However, proving the existence of the modulation structure from single X-ray diffraction was challenging because of the low-quality data from the as-grown crystals. Therefore, we performed a scanning/transmission electron microscopy (S/TEM) investigation of its microstructure. Figure S7(a) is a typical high angle annular dark field (HAADF) image of the specimen, where a huge amount of dislocation arrays with brighter contrast can be observed; these dense dislocations can be induced by the intrinsic Zn vacancies in the sample. The existence of such high defect level will affect mechanical properties of the single crystal, making it hard to perform large area structural analyses on it.

Figure 5(a) shows the selected area electron diffraction patterns (SAED), where the main diffraction spots can be well indexed to the average orthorhombic structure (space group $Pmnm$) along the [010] zone axis. Moreover, extra spots along \mathbf{c}^* are showing up as highlighted with a yellow arrow. These spots match the second order satellites spots, indicating the existence of modulation structure with a \mathbf{q} -vector having the \mathbf{c}^* component ~ 0.346 similar to $\text{KLaMn}_{1-x}\text{Te}_4$. These results are consistent with the single-crystal X-ray diffraction of $\text{KLaMn}_{1-x}\text{Te}_4$ sample.

Figure 5(b) displays the corresponding high-resolution TEM image of $\text{KLaZn}_{1-x}\text{Te}_4$. The measured interplanar d -spacings of (002), (200) and ($\bar{1}01$) planes in HRTEM are 2.31, 2.26, and 3.21 Å, respectively, in good agreement with the refinement results from PXRD.

Charge Transport Properties. Both $\text{KLaMn}_{1-x}\text{Te}_4$ and $\text{KLaZn}_{1-x}\text{Te}_4$ exhibit metallic behavior with moderately high resistivity near room temperature, see Figure 6(a). The resistivity of $\text{KLaZn}_{1-x}\text{Te}_4$ saturates to $\sim 26 \text{ m}\Omega \text{ cm}$ at 300 K whereas that of $\text{KLaMn}_{1-x}\text{Te}_4$ increases significantly below $\sim 50 \text{ K}$, indicating a semiconducting-like behavior at low temperature. The resistivity upturn does not obey an exponential growth with decreasing the temperature, see Figure S8. The resistivity values at room temperature for both $\text{KLaM}_{1-x}\text{Te}_4$ ($M = \text{Mn, Zn}$) are much larger than KLaCuTe_4 where there are no Cu vacancies in the $[\text{KCuTe}]$ layer.¹⁶⁻¹⁷ The larger values and low temperature upturn in resistivity are probably related to the massive random vacancies in the $[\text{KM}_{1-x}\text{Te}]$ layer acting as scattering centers. Hall resistivity data indicates that hole carriers dominate over the whole temperature range in $\text{KLaMn}_{1-x}\text{Te}_4$ and the carrier concentration with a magnitude of 10^{20} cm^{-3} slightly decreases with decreasing temperature, see Figure 6(b). The hole carrier concentration at 2 K ($1.1 \times 10^{20} \text{ cm}^{-3}$) is much smaller than the value ($7.0 \times 10^{20} \text{ cm}^{-3}$) in LaTe_3 at the same temperature³³ further supporting the scenario that electrons transfer from the $[\text{KMn}_{1-x}\text{Te}]$ block to the Te square nets in the $[\text{LaTe}_3]$ block.

The metallic character in $\text{KLaM}_{1-x}\text{Te}_4$ stems mainly from the 2D Te-square nets of the structure, which is known to be a metal despite the presence of the largely gapped CDW associated with the layer that contains the modulated square net.³¹⁻³² The $[\text{M}_{1-x}\text{Te}]$ component acts as an insulating layer as proved in the insulating behavior in $\text{BaFMn}_{0.5}\text{Te}$ with almost identical $[\text{Mn}_{1-x}\text{Te}]$ layer and will show unusual magnetic properties due to the local magnetic moment of Mn atoms.²⁰ The absence of obvious resistivity anomaly at the temperature where a spin glass freezing transition

from magnetic Mn atoms occurs at ~ 5 K (see magnetic properties below) for $\text{KLaMn}_{1-x}\text{Te}_4$ is consistent with the spatial separation and greater 2D character of the conduction electrons and localized spins in the structure. The non-zero electronic specific heat coefficients obtained from the heat capacity data, presented below for these two compounds, are consistent with a non-vanishing density of states at Fermi level as expected for metallic systems. The low temperature upturn in resistivity for the two compounds indicates that they are on the boundary of metal-insulator-transition possibly due to the Anderson localization³⁴⁻³⁵ originating from the disorder in these Q2D systems, just as the case in $\text{LaTe}_{1.95}$ with certain amount of Te vacancies in the Te square nets³⁶ while LaTe_3 without any intrinsic disorder shows metallic behavior all the way down to 2 K.³¹

Magnetic Properties

DC Magnetic Susceptibility. Temperature-dependent DC magnetic susceptibilities under ZFC and FC conditions with a magnetic field $H = 1000$ Oe applied in the ac plane for $\text{KLaMn}_{1-x}\text{Te}_4$ are shown in Figure 7(a). A significant bifurcation of ZFC and FC in the curve appears at ~ 5 K where there is a cusp feature in the ZFC curve. The cusp and bifurcation move to lower temperatures and the sharpness of the cusp is smoothed out when the applied magnetic fields increase, see Figure 7(b). The cusp in the ZFC curve is due to the SG freezing behavior which will be confirmed by the AC magnetic susceptibility below. The cusp point is called the spin freezing temperature T_f .³⁷ Field-dependent magnetization at 150 and 300 K shows a linear behavior from 0 to 7 T while it exhibits a non-linear behavior at 2 and 10 K, see Figure 7(c). The field-dependent magnetization at 2 K also shows small hysteresis at low magnetic fields with a coercive field of ~ 800 Oe, see the inset of Figure 7(c), consistent with the spin freezing scenario below T_f .

The magnetic susceptibility data in $\text{KLaMn}_{1-x}\text{Te}_4$ above 150 K can be well fit by a modified Curie-Weiss formula (the inset of Figure 7(a)): $\chi_0 + \frac{C}{T-\theta}$, where χ_0 is a constant value contributed by the temperature-independent diamagnetic part from electron orbital magnetism and the Pauli paramagnetic part from itinerant electrons in the system; C is a Curie constant from which effective magnetic moment for each unit can be calculated; θ is the Curie-Weiss temperature whose value indicates the effective magnetic interaction strength between those magnetic moments.³⁸⁻³⁹ The Curie-Weiss temperature θ obtained from the fitting is large and negative at -234 K, indicating strong antiferromagnetic interactions between Mn ions in the Mn-substructure at high temperatures but to a smaller degree than in $\text{BaFMn}_{0.5}\text{Te}$ (-557 K). The effective magnetic moment for each Mn atom is $2.58 \mu_B$, and is significantly smaller than the high spin state ($5.91 \mu_B$) for Mn^{2+} . Magnetic Mn ions in a tetrahedron $[\text{Mn}Q_4]$ ($Q = \text{S, Se, Te}$) usually show a high spin state as exemplified by many examples such as $\text{K}_6\text{Mn}Q_4$ ($Q = \text{S, Se, Te}$) ($\sim 5.9 \mu_B$)⁴⁰, $\text{BaFMn}_{0.5}\text{Te}$ ($\sim 6.0 \mu_B$)²⁰ and $A\text{MnTe}_2$ ($A = \text{K, Rb, Cs}$) ($\sim 4.3\text{-}4.9 \mu_B$).^{28, 41-42} The smaller magnetic moment in $\text{KLaMn}_{1-x}\text{Te}_4$ may be due to the significant hybridization of Mn- $3d$ and its ligand Te- $5p$ electrons as the case in the BaMn_2Pn_2 ($Pn = \text{P, As, Sb, Bi}$)⁴³⁻⁴⁶ and $A_2\text{Mn}_3\text{Se}_4$ ($A = \text{Rb, Cs}$).⁴⁷ The $[\text{KMn}_{1-x}\text{Te}]$ layer in $\text{KLaMn}_{1-x}\text{Te}_4$ is basically an insulating layer with localized Mn magnetic moments. It is intercalated between two metallic Te-square nets, which may increase the degree of itinerancy of $3d$ electrons of Mn ions in the $[\text{KMn}_{1-x}\text{Te}]$ insulating layer due to the proximity effect. Such a phenomenon has also been observed in the compound $\text{Sr}_2\text{Cr}_3\text{As}_3\text{O}_2$ ⁸ where the magnetic moment of the localized nature of Cr in the CrO_2 plane, sandwiched by two metallic Cr_2As_2 layers, is significantly reduced. Another scenario may be electron transfer between the Mn containing layer and the Te containing layer creating a small change in oxidation state in certain Mn atoms which reduces the overall average

effective moment. Such an electron transfer is implied by the heat capacity data below. The physical origin of the reduced magnetic effective moment in $\text{KLaMn}_{1-x}\text{Te}_4$ needs to be uncovered by further detailed investigations, which are beyond the study of this work.

When the magnetic field reaches 7 T the magnetization of $\text{KLaMn}_{1-x}\text{Te}_4$ at 2 K is only $0.12 \mu_{\text{B}}/\text{Mn}$, much smaller than magnetic moment of Mn ions ($\sim 2 \mu_{\text{B}}/\text{Mn}$) from the Curie-Weiss fitting mentioned above and points to antiferromagnetic interactions dominating between the Mn ions. The dominant antiferromagnetic interaction is also inferred from the field-dependent cusp temperature behavior shown above. A small bifurcation of the ZFC and FC curves appears at ~ 90 K, see Figure 7(a), which is also observed in our purest polycrystalline samples (Figure 7(d)). However, there is no anomaly at ~ 90 K in the magnetic susceptibility seen in less pure polycrystalline samples, see Figure S6 in SI. As a result, the anomaly is not intrinsic and probably arises from the magnetic transition from a tiny amount of MnTe_2 , whose magnetic transition happens to be at ~ 90 K.⁴⁸ The magnetic susceptibility data of the $\text{KLaZn}_{1-x}\text{Te}_4$ samples are essentially temperature-independent at high temperatures with an upturn from paramagnetic impurities at low temperatures, consistent with a metallic Pauli paramagnetic behavior and non-magnetic Zn^{2+} in this compound.

AC Magnetic Susceptibility. In order to prove the SG behavior in $\text{KLaMn}_{1-x}\text{Te}_4$ and further study its dynamic properties, frequency-dependent AC magnetic susceptibility measurements were used, see Figure 8. The real components of AC magnetic susceptibilities χ' , measured under different frequencies, have similar behavior to the DC magnetic susceptibility while the imaginary components χ'' , a quantity representing energy dissipation, start to grow rapidly at around the cusp temperature and drop again at lower temperatures, see Figure 8(a) and (b). The cusp temperature in χ' moves to higher values with increasing applied AC magnetic field frequency and below the

cusp temperature the value of χ' decreases, which are two typical characteristics of SG systems.³⁷ This cusp is called the spin freezing temperature T_f , see Figure 8(a). The edge where the value of χ'' increases rapidly also moves to higher temperature with increasing frequency, consistent with the case in χ' , see Figure 8(b). When a static magnetic $H = 500$ Oe is applied, the cusp temperature in χ' remains almost unchanged but it becomes broader, see Figure 8(c). As for χ'' , the transition point where χ'' increases rapidly does not change while the absolute value of χ'' is suppressed by a static magnetic field. Since the cusp is from the spin freezing scenario in the SG system, the static magnetic field cannot change the overall collective behavior where most of the magnetic moments freeze but it can decrease the magnetic response of freezing magnetic moments under an oscillating field. These observations suggest that the cusp temperature is attributed to an SG behavior in $\text{KLaMn}_{1-x}\text{Te}_4$.

In order to further reveal the characteristics of the SG behavior, T_f was extracted from the cusp position in each frequency in χ' , see Figure 9(a). A relative change of T_f with the magnitude of frequency is calculated as the following formula:³⁷

$$K = \frac{\Delta T_f}{T_f \log(\Delta f)}$$

This gives an estimated parameter K of ~ 0.064 , which is much larger than the canonical SG system such as $\text{Cu}_{1-x}\text{Mn}_x$ ($x \sim 1\%$) alloys ($K \sim 0.005$) with a very dilute concentration of Mn magnetic atoms but below the value in the normal superparamagnets ($K \sim 0.1-0.3$).^{37, 49} A critical slowing down approach was also employed to study its dynamic properties of SG in $\text{KLaMn}_{1-x}\text{Te}_4$ with the following equation^{37, 50}:

$$\tau = \tau_0 \left(\frac{T_f}{T_{SG}} - 1 \right)^{-z\nu}$$

where τ is the inverse of frequency f , τ_0 is the characteristic spin relaxation time, T_{SG} is the spin freezing temperature when frequency goes to zero, $z\nu$ is the dynamic critical exponent. The fitting by the above equation gives $z\nu = 11.7$, $\tau_0 = 2.17 \times 10^{-7}$ s and $T_{SG} = 4.48$ K, see Figure 9(b). The value of T_{SG} in a zero-frequency limit is consistent with the freezing temperature ($T_f \sim 5$ K) in the DC magnetic susceptibility. $z\nu$ falls in the range between 4 and 13 for a SG system.³⁷ τ_0 is much larger than the case in a canonical SG system which has a magnitude of $10^{-12} - 10^{-13}$ s, pointing to a rather slow spin dynamic relaxation process.³⁷ The above analysis supports the presence of cluster SG behavior in $\text{KLaMn}_{1-x}\text{Te}_4$ which is a natural consequence of its actual crystal structure and composition as explained below.

There are several ingredients that drive a system to SG behavior including randomness (disorder), competing interaction and magnetic frustration^{37, 49}, all of which are present in $\text{KLaMn}_{1-x}\text{Te}_4$. First, there are Mn vacancies randomly distributed in the $[\text{Mn}_{1-x}\text{Te}]$ ($x = 0.35$) layers. In fact, the ordered-Mn-vacancy compounds $A_2\text{Mn}_3\text{Se}_4$ ($A = \text{Rb}, \text{Cs}$)⁴⁷ and $\text{BaFMn}_{0.5}\text{Te}^{20}$ show antiferromagnetic order. Second, massive amount of Mn vacancies ($x \sim 0.35$) creating distributed Mn-Mn distances in the Mn sublattice, can lead to both antiferromagnetic and ferromagnetic interactions depending on the actual super-exchange path in the $[\text{Mn}_{1-x}\text{Te}]$ layer. As a result, competing interactions are expected to exist in the $[\text{Mn}_{1-x}\text{Te}]$ layers. In contrast to a canonical SG with diluted magnetic atoms such $\text{Cu}_{1-x}\text{Mn}_x$ alloys ($x \sim 1\%$)^{37, 49}, the Mn magnetic ions in $\text{KLaMn}_{1-x}\text{Te}_4$ are rather densely packed, making it possible to form magnetic clusters. A rather high spin relaxation time τ_0 observed in $\text{KLaMn}_{1-x}\text{Te}_4$ points to the existence of magnetic clusters because it will take a much longer time to drive large non-equilibrated magnetic clusters to equilibrated ones than the case in a single isolated magnetic ion.

Specific Heat. No obvious anomaly at ~ 5 K is observed in the specific heat data of $\text{KLaMn}_{1-x}\text{Te}_4$, see Figure 10(a), further supporting that the cusp in the magnetic susceptibility is due to a SG behavior rather than a classical magnetic phase transition. The low temperature specific heat in $\text{KLaZn}_{1-x}\text{Te}_4$ can be well described by the formula $\gamma T + \beta T^3 + \delta T^5$ where γT is the electronic specific heat and $\beta T^3 + \delta T^5$ is the phonon specific heat at low temperatures,⁵¹ see Figure 10(b). The obtained electronic coefficient $\gamma = 3.7 \text{ mJ K}^{-2} \text{ mol-fu}^{-1}$ is larger than that in LaTe_3 ($1.1 \text{ mJ K}^{-2} \text{ mol-fu}^{-1}$)³¹ normalizing for the same number of LaTe_3 layers in the formula. This result is consistent with electron transfer from the $[\text{KZn}_{1-x}\text{Te}]$ to $[\text{LaTe}_3]$ layer and most likely to the Te-square net, creating a self-doping scenario in $\text{KLaZn}_{1-x}\text{Te}_4$. Since the main oxidation state of Mn element in $\text{KLaMn}_{1-x}\text{Te}_4$ is almost the same as Zn element in $\text{KLaZn}_{1-x}\text{Te}_4$, electron transfer from $[\text{KMn}_{1-x}\text{Te}]$ to $[\text{LaTe}_3]$ also exists. The estimated Debye temperature $\Theta = 181$ K from the equation $\Theta = \left(\frac{12NR\pi^4}{5\beta}\right)^{1/3}$ is very close to LaTe_3 ³¹ which is reasonable as they share the same building blocks and have a similar phonon spectrum.

Since $\text{KLaZn}_{1-x}\text{Te}_4$ and $\text{KLaMn}_{1-x}\text{Te}_4$ have the same crystal structure and the mass difference between Zn and Mn atoms is small, their phonon specific heat will be very similar. They have the same electron counts in the Te-square nets suggesting that they should also have similar electronic specific heat. Therefore, the total specific heat of $\text{KLaZn}_{1-x}\text{Te}_4$ will be a good approximation to the non-magnetic contribution in $\text{KLaMn}_{1-x}\text{Te}_4$ at low temperature. The magnetic specific heat was obtained by subtracting the specific heat of $\text{KLaZn}_{1-x}\text{Te}_4$ from that of $\text{KLaMn}_{1-x}\text{Te}_4$, see Figure 10(c). A broad peak in C_m/T appears at ~ 20 K, much higher than T_f . This indicates that magnetic entropy loss happens way above T_f , which is a typical feature of a SG system.^{37, 49} The integrated magnetic entropy is approaching the theoretical value of a spin-1 system $R\ln(3)$ with increasing

temperature, see Figure 10(d). Therefore, the specific heat data confirm the metallic behavior in $\text{KLaZn}_{1-x}\text{Te}_4$ and supports a SG behavior in $\text{KLaMn}_{1-x}\text{Te}_4$.

Conclusions

Two Q2D heterostructures $\text{KLaM}_{1-x}\text{Te}_4$ ($M = \text{Mn}, \text{Zn}$) were successfully synthesized, composed of practically lattice-matched alternating $[\text{LaTe}_3]$ and $[\text{KM}_{1-x}\text{Te}]$ layers. Electron transfer from $[\text{KM}_{1-x}\text{Te}]$ to $[\text{LaTe}_3]$ layers exists creating a self-doping effect, and at the same time maybe serving to stabilize the structures because the charge transfer between the layers is driven by their different chemical potential levels and modulates the Fermi energy of the $[\text{LaTe}_3]$ affecting the details of Fermi surface nesting and the \mathbf{q} -vector. $\text{KLaMn}_{1-x}\text{Te}_4$ exhibits CDW order with $\mathbf{q} = 1/2\mathbf{b}^* + 0.3478\mathbf{c}^*$ at room temperature originating from electronic instability of Te-square nets, and cluster SG behavior with $T_f \approx 5$ K coming from disordered $[\text{Mn}_{1-x}\text{Te}]$ layers. In-plane lattice match and chemical compatibility between two functional layers are important to stabilize the strong interlayer bonding hetero-layered structures and this feature can be a viable basis for targeting productive synthesis directions for hetero-structural compounds.

ASSOCIATED CONTENT

Supporting Information.

This material is available free of charge via the Internet at <http://pubs.acs.org>.

Figure S1: PXRD experimental patterns of polycrystalline samples of $\text{KLaMn}_{1-x}\text{Te}_4$ and $\text{KLaZn}_{1-x}\text{Te}_4$ and their simulated patterns of $\text{KLaMn}_{1-x}\text{Te}_4$ and MnTe_2 . Figure S2: PXRD pattern of $\text{KLaZn}_{1-x}\text{Te}_4$ sample exposed in air for two days and simulated pattern of Te element. Figure S3: one energy dispersive spectroscopy (EDS) data of $\text{KLaMn}_{1-x}\text{Te}_4$. Figure S4: Specific heat data of two $\text{KLaMn}_{1-x}\text{Te}_4$.

$x\text{Te}_4$ and two $\text{KLaZn}_{1-x}\text{Te}_4$ samples. Figure S5: electric contacts created by Pt sputtering and silver paste for transport property measurements. Figure S6: magnetic susceptibility from another batch of $\text{KLaMn}_{1-x}\text{Te}_4$ polycrystalline sample. Figure S7: high angle annular dark field image and its corresponding EDS mapping of $\text{KLaZn}_{1-x}\text{Te}_4$ Table S1-5: detailed modulation structure parameters of $\text{KLaMn}_{1-x}\text{Te}_4$. Experimental details of charge transport property, energy-dispersive X-ray spectroscopy and scanning and transmission electron microscopy measurements. A cif file of the modulated structure.

AUTHOR INFORMATION

Corresponding Author

*E-mail: m-kanatzidis@northwestern.edu

Notes

The authors declare no competing financial interest.

Acknowledgements

This work was supported primarily by the U.S. Department of Energy, Office of Science, Basic Energy Sciences, Materials Sciences and Engineering. Use of the Center for Nanoscale Materials, an Office of Science user facility, at Argonne National Laboratory was supported by the U.S. Department of Energy, Office of Science, Office of Basic Energy Sciences, under Contract No. DE-AC02-06CH11357. TEM work was performed by use of the EPIC, Keck-II, and/or SPID facility of Northwestern University's NUANCE Center, which has received support from the Soft and Hybrid Nanotechnology Experimental (SHyNE) Resource (NSF ECCS-1542205); the MRSEC program (DMR-1720139) at the Materials Research Center; the International Institute for

Nanotechnology (IIN); the Keck Foundation; and the State of Illinois, through the IIN. This work was supported in part by the National Science Foundation through the MRSEC program (NSF-DMR 1720139) at the Materials Research Center (V.P. Dravid, electron microscopy investigation). J.-K. Bao acknowledges the Alexander von Humboldt Foundation for financial support in Germany.

References

- (1) Bednorz, J. G.; Müller, K. A., Possible high T_c superconductivity in the Ba–La–Cu–O system. *Z. Phys. B: Condens. Matter* **1986**, *64*, 189-193.
- (2) Kamihara, Y.; Watanabe, T.; Hirano, M.; Hosono, H., Iron-Based Layered Superconductor $\text{La}[\text{O}_{1-x}\text{F}_x]\text{FeAs}$ ($x = 0.05\text{--}0.12$) with $T_c = 26$ K. *J. Am. Chem. Soc* **2008**, *130*, 3296-3297.
- (3) Hamlin, J. J.; Zocco, D. A.; Sayles, T. A.; Maple, M. B.; Chu, J. H.; Fisher, I. R., Pressure-Induced Superconducting Phase in the Charge-Density-Wave Compound Terbium Tritelluride. *Phys. Rev. Lett.* **2009**, *102*, 177002.
- (4) Paglione, J.; Greene, R. L., High-temperature superconductivity in iron-based materials. *Nat. Phys.* **2010**, *6*, 645-658.
- (5) Liu, Y.; Liu, Y.-B.; Tang, Z.-T.; Jiang, H.; Wang, Z.-C.; Ablimit, A.; Jiao, W.-H.; Tao, Q.; Feng, C.-M.; Xu, Z.-A., et al., Superconductivity and ferromagnetism in hole-doped $\text{RbEuFe}_4\text{As}_4$. *Phys. Rev. B: Condens. Matter Mater. Phys.* **2016**, *93*, 214503.
- (6) Smylie, M. P.; Willa, K.; Bao, J. K.; Ryan, K.; Islam, Z.; Claus, H.; Simsek, Y.; Diao, Z.; Rydh, A.; Koshelev, A. E., et al., Anisotropic superconductivity and magnetism in single-crystal $\text{RbEuFe}_4\text{As}_4$. *Phys. Rev. B: Condens. Matter Mater. Phys.* **2018**, *98*, 104503.
- (7) Chen, C.-W.; Wang, W.; Loganathan, V.; Carr, S. V.; Harriger, L. W.; Georgen, C.; Nevidomskyy, A. H.; Dai, P.; Huang, C. L.; Morosan, E., Possible Mott transition in layered $\text{Sr}_2\text{Mn}_3\text{As}_2\text{O}_2$ single crystals. *Phys. Rev. B: Condens. Matter Mater. Phys.* **2019**, *99*, 144423.
- (8) Liu, J.; Wang, J.; Sheng, J.; Ye, F.; Taddei, K. M.; Fernandez-Baca, J. A.; Luo, W.; Sun, G.-A.; Wang, Z.-C.; Jiang, H., et al., Neutron diffraction study on magnetic structures and transitions in $\text{Sr}_2\text{Cr}_3\text{As}_2\text{O}_2$. *Phys. Rev. B: Condens. Matter Mater. Phys.* **2018**, *98*, 134416.
- (9) Wieggers, G. A., Misfit layer compounds: Structures and physical properties. *Prog. Solid State Chem.* **1996**, *24*, 1-139.
- (10) Alemayehu, M. B.; Ta, K.; Falmbigl, M.; Johnson, D. C., Structure, Stability, and Properties of the Intergrowth Compounds $([\text{SnSe}]_{1+\delta})_m(\text{NbSe}_2)_n$, where $m = n = 1\text{--}20$. *J. Am. Chem. Soc.* **2015**, *137*, 4831-4839.
- (11) Yao, Q.; Shen, D. W.; Wen, C. H. P.; Hua, C. Q.; Zhang, L. Q.; Wang, N. Z.; Niu, X. H.; Chen, Q. Y.; Dudin, P.; Lu, Y. H., et al., Charge Transfer Effects in Naturally Occurring van der Waals Heterostructures $(\text{PbSe})_{1.16}(\text{TiSe}_2)_m$ ($m = 1, 2$). *Phys. Rev. Lett.* **2018**, *120*, 106401.

- (12) Leriche, R. T.; Palacio-Morales, A.; Campetella, M.; Tresca, C.; Sasaki, S.; Brun, C.; Debontridder, F.; David, P.; Arfaoui, I.; Šofranko, O., et al., Misfit Layer Compounds: A Platform for Heavily Doped 2D Transition Metal Dichalcogenides. *Adv. Funct. Mater.* **2020**, 2007706.
- (13) Clarke, S. J.; Adamson, P.; Herkelrath, S. J. C.; Rutt, O. J.; Parker, D. R.; Pitcher, M. J.; Smura, C. F., Structures, Physical Properties, and Chemistry of Layered Oxychalcogenides and Oxy pnictides. *Inorg. Chem.* **2008**, *47*, 8473-8486.
- (14) Jiang, H.; Sun, Y.-L.; Xu, Z.-A.; Cao, G.-H., Crystal chemistry and structural design of iron-based superconductors. *Chin. Phys. B* **2013**, *22*, 087410.
- (15) Malliakas, C. D.; Kanatzidis, M. G., Divergence in the Behavior of the Charge Density Wave in $RETe_3$ (RE = Rare-Earth Element) with Temperature and RE Element. *J. Am. Chem. Soc.* **2006**, *128*, 12612-12613.
- (16) Patschke, R.; Heising, J.; Kanatzidis, M.; Brazis, P.; Kannewurf, C. R., $KCuCeTe_4$: A New Intergrowth Rare Earth Telluride with an Incommensurate Superstructure Associated with a Distorted Square Net of Tellurium. *Chem. Mater.* **1998**, *10*, 695-697.
- (17) Malliakas, C. D.; Kanatzidis, M. G., Charge Density Waves in the Square Nets of Tellurium of $AMRETe_4$ (A = K, Na; M = Cu, Ag; RE = La, Ce). *J. Am. Chem. Soc.* **2007**, *129*, 10675-10677.
- (18) X-AREA, X-SHAPE, and X-RED; STOE and Cie GmbH, Darmstadt, Germany, 2009.
- (19) Petříček, V.; Dušek, M.; Palatinus, L., Crystallographic Computing System JANA2006: General features. *Z. Kristallogr. - Cryst. Mater.* **2014**, *229*, 345.
- (20) Chen, H.; McClain, R.; He, J.; Zhang, C.; Olding, J. N.; dos Reis, R.; Bao, J.-K.; Hadar, I.; Spanopoulos, I.; Malliakas, C. D., et al., Antiferromagnetic Semiconductor $BaFMn_{0.5}Te$ with Unique Mn Ordering and Red Photoluminescence. *J. Am. Chem. Soc.* **2019**, *141*, 17421-17430.
- (21) Parker, D. R.; Pitcher, M. J.; Baker, P. J.; Franke, I.; Lancaster, T.; Blundell, S. J.; Clarke, S. J., Structure, antiferromagnetism and superconductivity of the layered iron arsenide $NaFeAs$. *Chem. Commun. (Cambridge, U. K.)* **2009**, 2189-2191.
- (22) Lompwsky, L.; Bronger, W., Synthese und Kristallstruktur von $KMnP$ und $KMnAs$. *Z. Anorg. Allg. Chem.* **1974**, *409*, 221-227.
- (23) Finlayson, D. M.; Greig, D.; Llewellyn, J. P.; Smith, T., Some Electrical Characteristics of Single Crystal Iron Monotelluride. *Proc. Phys. Soc., London, Sect. B* **1956**, *69*, 860-862.
- (24) Moelo, Y.; Meerschaut, A.; Rouxel, J.; Auriel, C., Precise analytical characterization of incommensurate sandwiched layered compounds $[(Pb,Sn)S]_{1+x}[(Nb,Ti)S_2]_m$ ($0.08 \leq x \leq 0.28$, $m = 1 - 3$). Role of cationic coupling on the properties and the structural modulation. *Chem. Mater.* **1995**, *7*, 1759-1771.
- (25) Cario, L.; Palvadeau, P.; Lafond, A.; Deudon, C.; Moëlo, Y.; Corraze, B.; Meerschaut, A., Mixed-Valence State of Europium in the Misfit Layer Compound $(EuS)_{1.173}NbS_2$. *Chem. Mater.* **2003**, *15*, 943-950.
- (26) Kalläne, M.; Rossnagel, K.; Marczyński-Bühlow, M.; Kipp, L.; Starnberg, H. I.; Stoltz, S. E., Stabilization of the Misfit Layer Compound $(PbS)_{1.13}TaS_2$ by Metal Cross Substitution. *Phy. Rev. Lett.* **2008**, *100*, 065502.
- (27) Shao, Y.-T.; Wang, Z.-C.; Li, B.-Z.; Wu, S.-Q.; Wu, J.-F.; Ren, Z.; Qiu, S.-W.; Rao, C.; Wang, C.; Cao, G.-H., $BaTh_2Fe_4As_4(N_{0.7}O_{0.3})_2$: An iron-based superconductor stabilized by inter-block-layer charge transfer. *Sci. China Mater.* **2019**, *62*, 1357-1362.
- (28) Kim, J.; Wang, C.; Hughbanks, T., Synthesis and Structures of New Layered Ternary Manganese Tellurides: $AMnTe_2$ (A = K, Rb, Cs), $Na_3Mn_4Te_6$, and $NaMn_{1.56}Te_2$. *Inorg. Chem.* **1999**, *38*, 235-242.

- (29) Wang, Z.-C.; He, C.-Y.; Wu, S.-Q.; Tang, Z.-T.; Liu, Y.; Ablimit, A.; Feng, C.-M.; Cao, G.-H., Superconductivity in $\text{KCa}_2\text{Fe}_4\text{As}_4\text{F}_2$ with Separate Double Fe_2As_2 Layers. *J. Am. Chem. Soc* **2016**, *138*, 7856-7859.
- (30) Wu, S.-Q.; Wang, Z.-C.; He, C.-Y.; Tang, Z.-T.; Liu, Y.; Cao, G.-H., Superconductivity at 33-37 K in $\text{ALn}_2\text{Fe}_4\text{As}_4\text{O}_2$ ($A = \text{K}$ and Cs ; $\text{Ln} =$ lanthanides). *Phys. Rev. Mater.* **2017**, *1*, 044804.
- (31) Ru, N.; Fisher, I. R., Thermodynamic and transport properties of YTe_3 , LaTe_3 , and CeTe_3 . *Phys. Rev. B: Condens. Matter Mater. Phys.* **2006**, *73*, 033101.
- (32) Brouet, V.; Yang, W. L.; Zhou, X. J.; Hussain, Z.; Moore, R. G.; He, R.; Lu, D. H.; Shen, Z. X.; Laverock, J.; Dugdale, S. B., et al., Angle-resolved photoemission study of the evolution of band structure and charge density wave properties in $R\text{Te}_3$ ($R = \text{Y}$, La , Ce , Sm , Gd , Tb , and Dy). *Phys. Rev. B: Condens. Matter Mater. Phys.* **2008**, *77*, 235104.
- (33) Pariari, A.; Koley, S.; Roy, S.; Singha, R.; Laad, M. S.; Taraphder, A.; Mandal, P., Fascinating interplay between Charge Density Wave Order and magnetic field in Non-magnetic Rare-Earth Tritelluride LaTe_3 . *arXiv preprint arXiv:1901.08267* **2019**.
- (34) Anderson, P. W., Absence of Diffusion in Certain Random Lattices. *Phys. Rev.* **1958**, *109*, 1492-1505.
- (35) Dynes, R. C., LOCALIZATION AND THE METAL-INSULATOR TRANSITION — EXPERIMENTAL OBSERVATIONS. *Int. J. Mod. Phys. B* **2010**, *24*, 2072-2089.
- (36) Shin, K. Y.; Brouet, V.; Ru, N.; Shen, Z. X.; Fisher, I. R., Electronic structure and charge-density wave formation in $\text{LaTe}_{1.95}$ and $\text{CeTe}_{2.00}$. *Phys. Rev. B: Condens. Matter Mater. Phys.* **2005**, *72*, 085132.
- (37) Mydosh, J. A., *Spin Glasses: An Experimental Introduction*. Taylor and Francis: London, 1993.
- (38) Johnston, D. C., The puzzle of high temperature superconductivity in layered iron pnictides and chalcogenides. *Adv. Phys.* **2010**, *59*, 803-1061.
- (39) Bao, J.-K.; Tang, Z.-T.; Jung, H. J.; Liu, J.-Y.; Liu, Y.; Li, L.; Li, Y.-K.; Xu, Z.-A.; Feng, C.-M.; Chen, H., et al., Unique $[\text{Mn}_6\text{Bi}_5]^-$ Nanowires in KMn_6Bi_5 : A Quasi-One-Dimensional Antiferromagnetic Metal. *J. Am. Chem. Soc* **2018**, *140*, 4391-4400.
- (40) Bronger, W.; Müller, P., The magnetochemical characterisation of the bonding features in ternary chalcogenides of manganese, iron and cobalt with low dimensional structural units. *J. Alloys Compd.* **1997**, *246*, 27-36.
- (41) Kim, J.; Hughbanks, T., Synthesis and Structures of New Layered Ternary Manganese Selenides: AMnSe_2 ($A = \text{Li}$, Na , K , Rb , Cs) and $\text{Na}_2\text{Mn}_2\text{Se}_3$. *J. Solid State Chem.* **1999**, *146*, 217-225.
- (42) Kim, J.; Wang, C.; Hughbanks, T., Synthesis and Structures of New Layered Ternary Manganese Tellurides: AMnTe_2 ($A = \text{Li}$, Na). *Inorg. Chem.* **1998**, *37*, 1428-1429.
- (43) Brock, S. L.; Greedan, J. E.; Kauzlarich, S. M., Resistivity and Magnetism of AMn_2P_2 ($A = \text{Sr}$, Ba): The Effect of Structure Type on Physical Properties. *J. Solid State Chem.* **1994**, *113*, 303-311.
- (44) Singh, Y.; Green, M. A.; Huang, Q.; Kreyssig, A.; McQueeney, R. J.; Johnston, D. C.; Goldman, A. I., Magnetic order in BaMn_2As_2 from neutron diffraction measurements. *Phys. Rev. B: Condens. Matter Mater. Phys.* **2009**, *80*, 100403.
- (45) Zhang, Q.; Diao, Z.; Cao, H.; Saleheen, A.; Chapai, R.; Gong, D.; Stadler, S.; Jin, R., Structure-property relationship in layered BaMn_2Sb_2 and $\text{Ba}_2\text{Mn}_3\text{Sb}_2\text{O}_2$. *Phys. Rev. B: Condens. Matter Mater. Phys.* **2019**, *99*, 184416.

- (46) Calder, S.; Saporov, B.; Cao, H. B.; Niedziela, J. L.; Lumsden, M. D.; Sefat, A. S.; Christianson, A. D., Magnetic structure and spin excitations in BaMn₂Bi₂. *Phys. Rev. B: Condens. Matter Mater. Phys.* **2014**, *89*, 064417.
- (47) Bronger, W.; Hardtdegen, H.; Kanert, M.; Müller, P.; Schmitz, D., Alkalimanganselenide und -telluride A₂Mn₃X₄ – Synthese, Kristall- und Spinstruktur. *Z. Anorg. Allg. Chem.* **1996**, *622*, 313-318.
- (48) Burllet, P.; Ressouche, E.; Malaman, B.; Welter, R.; Sanchez, J. P.; Vulliet, P., Noncollinear magnetic structure of MnTe₂. *Phys. Rev. B: Condens. Matter Mater. Phys.* **1997**, *56*, 14013-14018.
- (49) Mydosh, J. A., Spin glasses: redux: an updated experimental/materials survey. *Rep. Prog. Phys.* **2015**, *78*, 052501.
- (50) Binder, K.; Young, A. P., Spin glasses: Experimental facts, theoretical concepts, and open questions. *Rev. Mod. Phys.* **1986**, *58*, 801-976.
- (51) Cetas, T. C.; Tilford, C. R.; Swenson, C. A., Specific Heats of Cu, GaAs, GaSb, InAs, and InSb from 1 to 30 K. *Phys. Rev.* **1968**, *174*, 835-844.

Table 1. Crystal data and structure refinement for KLaMn_{1-x}Te₄ at 293 K.

Empirical formula	KLaMn _{0.65} Te ₄
Formula weight	724.1 g mol ⁻¹
Temperature	293 K
Wavelength	0.71075 Å
Crystal system	orthorhombic
Space group	<i>Pmnm</i> (01/2 γ)s00
Unit cell dimensions	$a = 4.4815(3)$ Å, $\alpha = 90^\circ$ $b = 21.6649(16)$ Å, $\beta = 90^\circ$ $c = 4.5220(3)$ Å, $\gamma = 90^\circ$
q -vector(1)	$1/2\mathbf{b}^* + 0.3478(3)\mathbf{c}^*$
Volume	439.05(5) Å ³
<i>Z</i>	2
Density (calculated)	5.4774 g cm ⁻³
Absorption coefficient	19.157 mm ⁻¹
<i>F</i> (000)	601
Crystal size	0.13 × 0.10 × 0.007 mm ³
θ range for data collection	2.82 to 29.2°
Index ranges	$-6 \leq h \leq 6$, $-30 \leq k \leq 30$, $-6 \leq l \leq 6$, $-2 \leq m \leq 2$
Reflections collected	18531 (4014 main + 14517 satellites)
Independent reflections	3087 (716 main + 2371 satellites) [<i>R</i> _{int} = 0.0275]
Completeness to $\theta = 29.2^\circ$	99%
Refinement method	Full-matrix least-squares on <i>F</i> ²
Data / constrains / restraints / parameters	3087 / 0 / 0 / 89
Goodness-of-fit on <i>F</i> ²	3.22
Final <i>R</i> indices [<i>I</i> > 2 σ (<i>I</i>)]	<i>R</i> _{obs} = 0.0535, <i>wR</i> _{obs} = 0.1317
<i>R</i> indices [all data]	<i>R</i> _{all} = 0.0728, <i>wR</i> _{all} = 0.1341
Final <i>R</i> main indices [<i>I</i> > 2 σ (<i>I</i>)]	<i>R</i> _{obs} = 0.0385, <i>wR</i> _{obs} = 0.0912
<i>R</i> main indices (all data)	<i>R</i> _{all} = 0.0390, <i>wR</i> _{all} = 0.0912
Final <i>R</i> 1 st order satellites [<i>I</i> > 2 σ (<i>I</i>)]	<i>R</i> _{obs} = 0.1049, <i>wR</i> _{obs} = 0.2122
<i>R</i> 1 st order satellites (all data)	<i>R</i> _{all} = 0.1451, <i>wR</i> _{all} = 0.2146
Extinction coefficient	0.2250(150)
<i>T</i> _{min} and <i>T</i> _{max} coefficients	0.0949 and 0.8553
Largest diff. peak and hole	4.51 and -4.01 e ⁻ Å ⁻³

$$R = \frac{\sum ||F_o| - |F_c||}{\sum |F_o|}, wR = \left\{ \frac{\sum [w(|F_o|^2 - |F_c|^2)^2]}{\sum [w(|F_o|^4)]} \right\}^{1/2} \text{ and } w = 1/(\sigma^2(I) + 0.0004I^2)$$

Figures and Captions

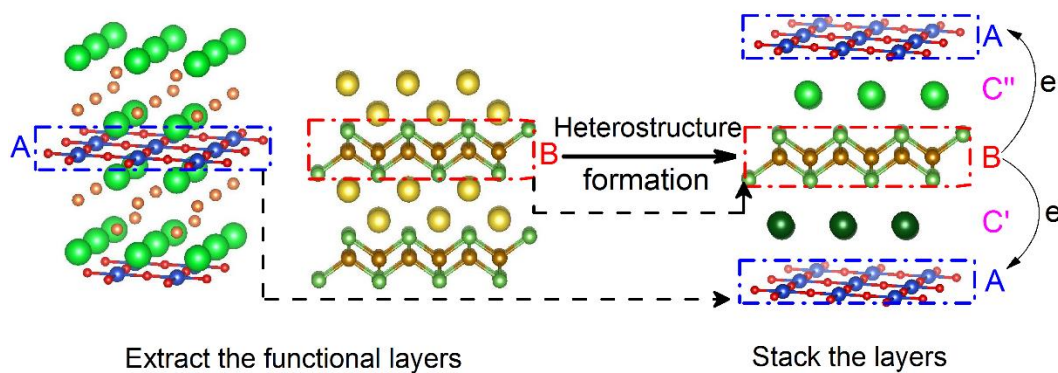


Figure 1. Schematic illustration of deriving heterolayered compounds. Certain crystal structure slabs A, B stable in parent compounds serve as the components in intergrowth compounds AB. The C layers show are generally charge-balancing counterions. Electron transfer between functional layers A and B can happen if they have different chemical potential levels, creating a self-doping effect.

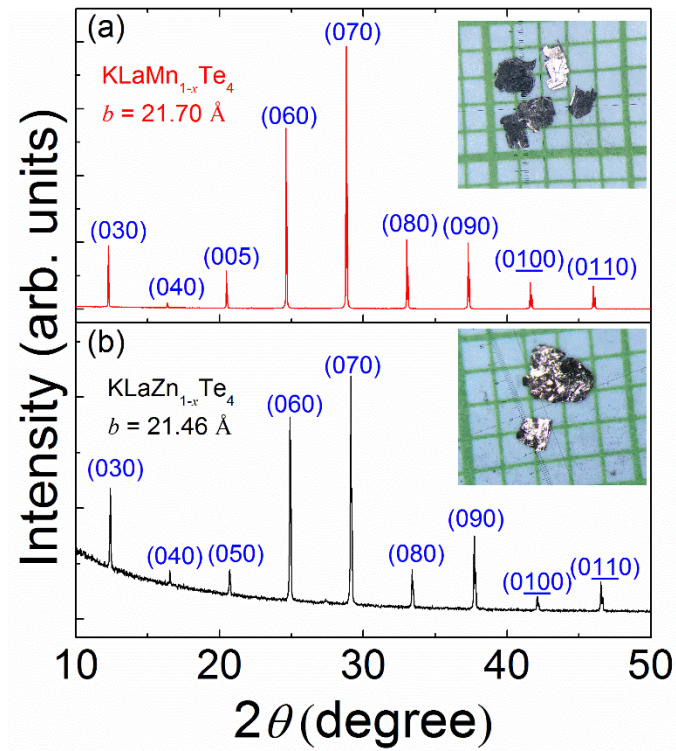


Figure 2. (a), (b) X-ray diffraction patterns of single crystals indexed by $(0k0)$ reflections as well as pictures of single crystals under the optical microscope for $\text{KLaMn}_{1-x}\text{Te}_4$ and $\text{KLaZn}_{1-x}\text{Te}_4$, respectively.

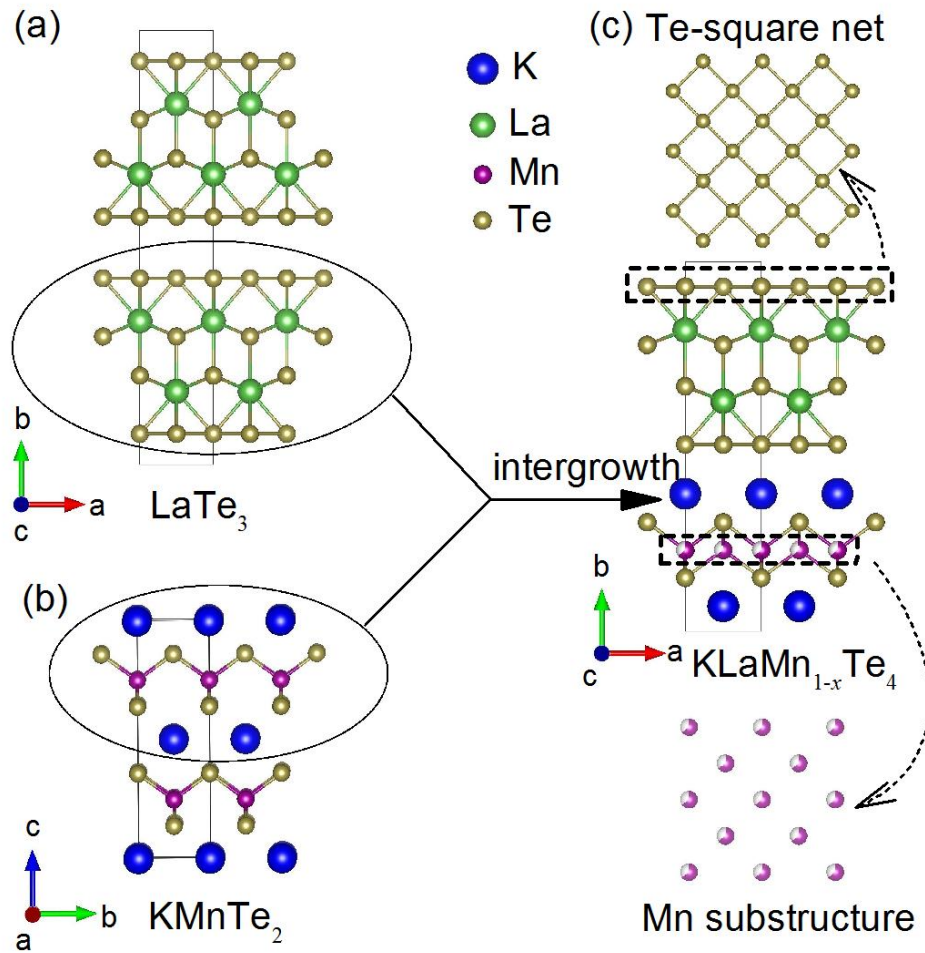


Figure 3. (a), (b) Crystal structures of LaTe_3 and KMnTe_2 , respectively. (c) Average crystal structure of heterolayer compound $\text{KLaMn}_{1-x}\text{Te}_4$. Te-square nets and Mn substructure with vacancies shown in the upper and lower part of the panel, respectively.

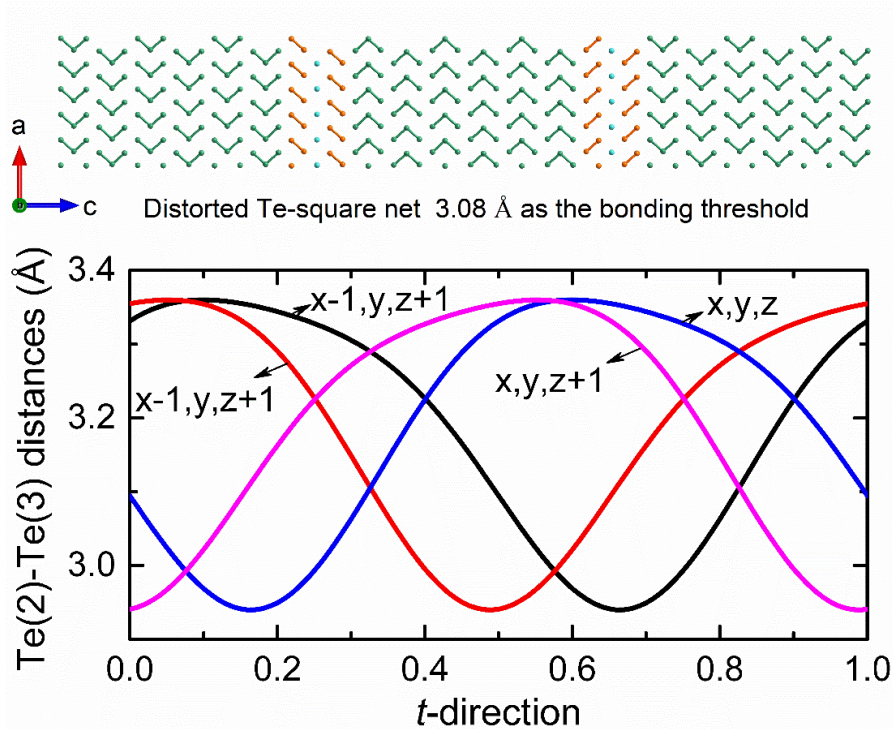


Figure 4. Upper panel: the pattern of monomers, dimers and trimers of Te atoms using the Te-Te bonding distance threshold of 3.08 Å in the distorted Te-square net. Lower panel: Te(2)-Te(3) distance with the modulation wave phase t . each Te(2) atom has four nearest Te(3) atoms.

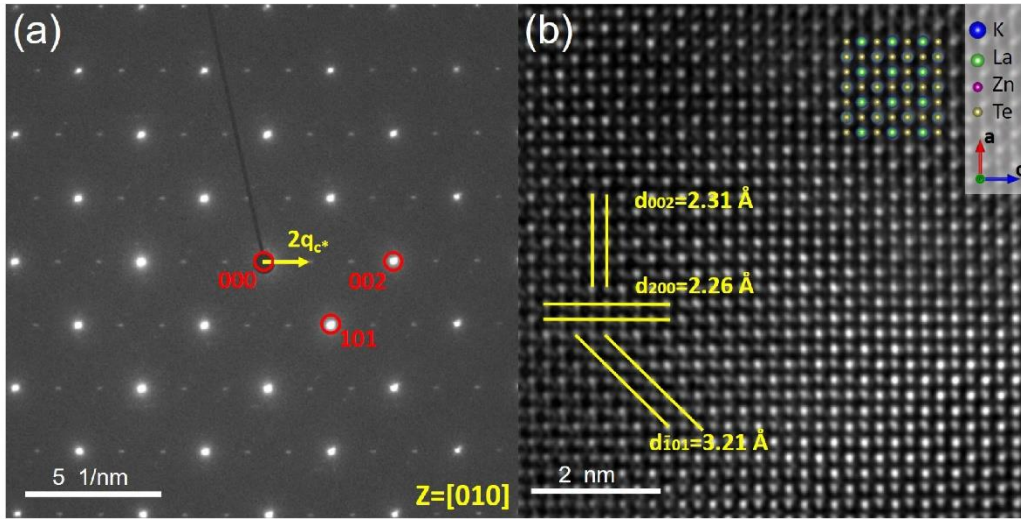


Figure 5. (a) Selected area electron diffraction (SAED) patterns of $\text{KLaZn}_{1-x}\text{Te}_4$ along the $[010]$ zone axis. The indices of main reflections are based on the orthorhombic average structure (space group $Pmnm$). Satellite reflections with a second order are observed along \mathbf{c}^* as labelled as $2\mathbf{q}_{\mathbf{c}^*}$, indicating the existence of modulation structure. (b) HRTEM of $\text{KLaZn}_{1-x}\text{Te}_4$ along the $[010]$ zone axis with some lattice planes and their corresponding distances marked. The structure schematic is overlaid on the upper right corner.

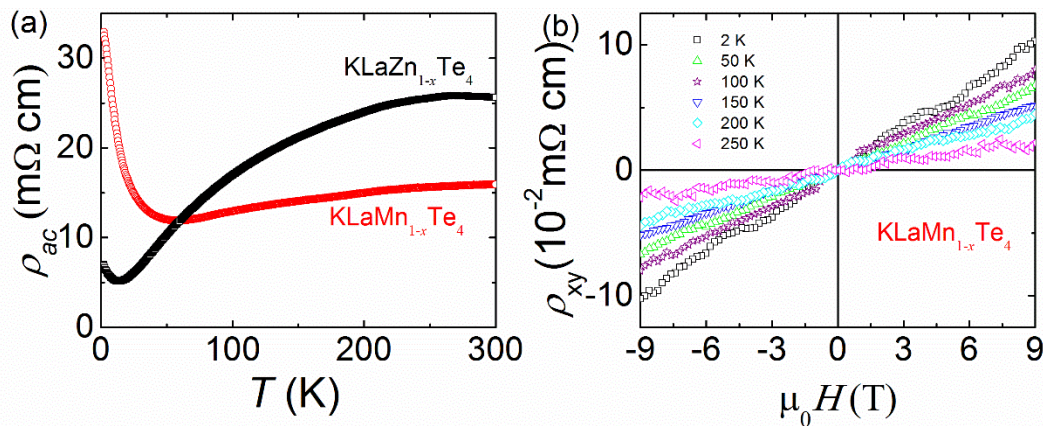


Figure 6. (a) Temperature dependence of resistivity in the ac plane for $\text{KLaMn}_{1-x}\text{Te}_4$ and $\text{KLaZn}_{1-x}\text{Te}_4$ single crystals. (b) Field-dependent Hall resistivity under different temperatures.

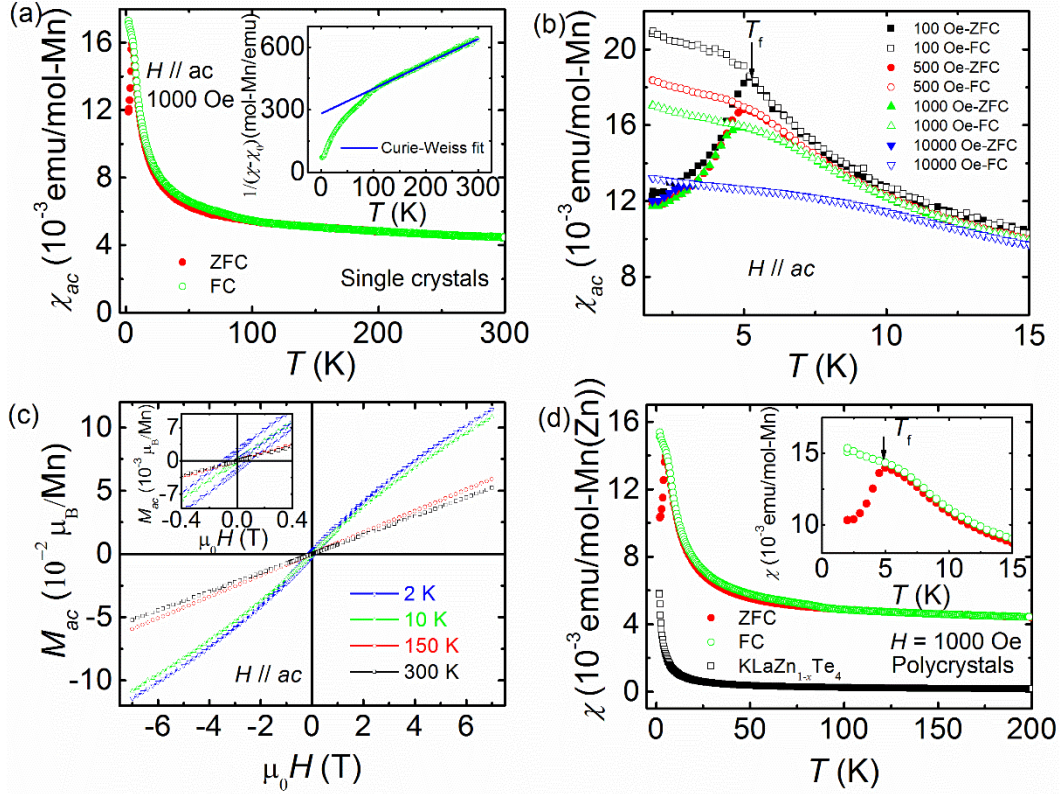


Figure 7. (a) Temperature-dependent magnetic susceptibilities of $\text{KLaMn}_{1-x}\text{Te}_4$ with applied fields (1000 Oe) in the ac plane under zero-field-cooled (ZFC) and field-cooled (FC) procedures. Inset shows the plot of $1/(\chi-\chi_0)$ vs T for FC data with the blue dashed line as the Curie-Weiss fit above 150 K. (b) Temperature-dependent magnetic susceptibilities of $\text{KLaMn}_{1-x}\text{Te}_4$ under different magnetic fields. (c) Isothermal magnetizations versus fields at different temperatures. The inset shows the magnetizations under small magnetic fields. (d) Temperature-dependent magnetic susceptibilities of polycrystalline sample $\text{KLaMn}_{1-x}\text{Te}_4$ (circle symbol) under ZFC and FC procedures and $\text{KLaZn}_{1-x}\text{Te}_4$ (square symbol) under ZFC procedure. Inset shows the cusp feature below 15 K for $\text{KLaMn}_{1-x}\text{Te}_4$.

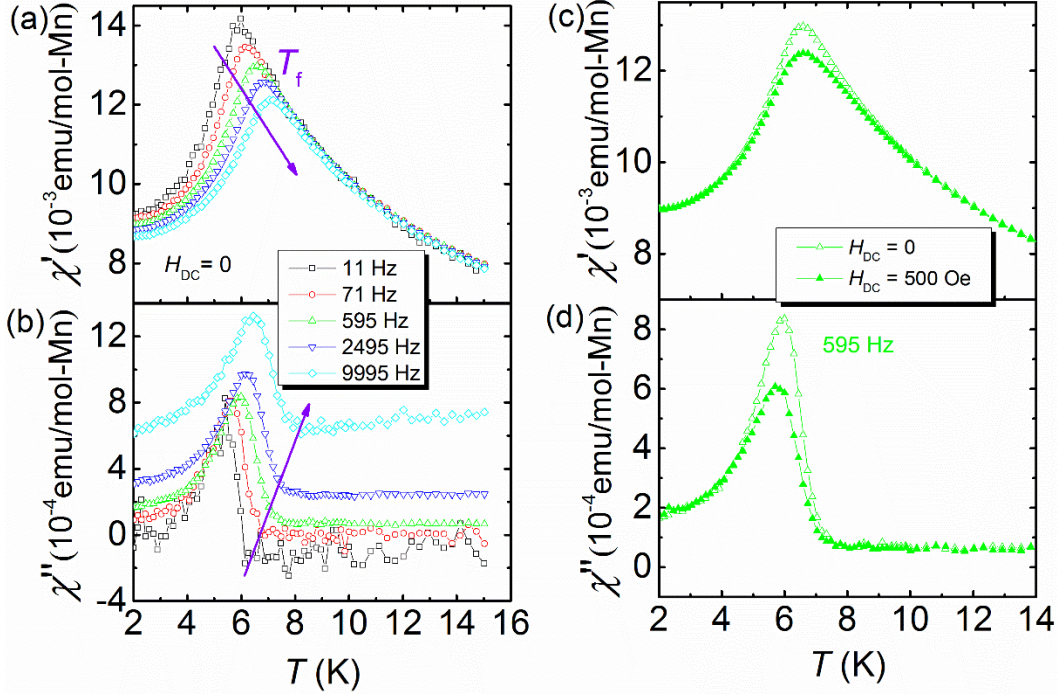


Figure 8. (a), (b) Real (χ') and imaginary (χ'') components of temperature-dependent AC magnetic susceptibility with zero static magnetic field $H_{DC} = 0$ under different frequencies spanning from 11 to 9995 Hz. Some curves under certain frequencies are not shown to make the trend of the freezing temperature easy to identify. (c), (d) Temperature-dependent χ' and χ'' with both $H_{DC} = 0$ and 500 Oe under the same frequency of 595 Hz.

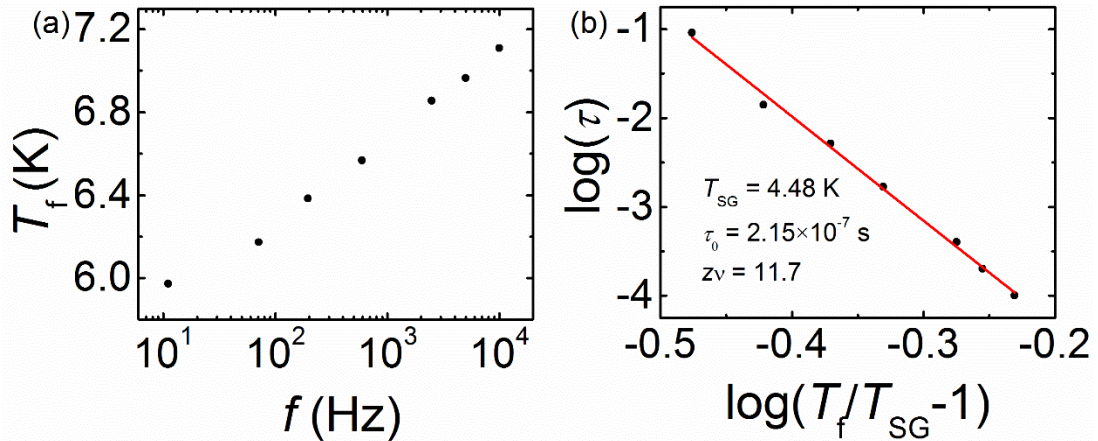


Figure 9. (a) Frequency-dependent freezing temperatures T_f extracted from the cusp temperatures in the real (χ') component of AC magnetic susceptibility. The axis of frequency is plotted as a log scale. (b) Critical slowing down plot with the formula $\tau = \tau_0 \left(\frac{T_f}{T_{SG}} - 1 \right)^{-z\nu}$. The red line is the fit for the experimental data.

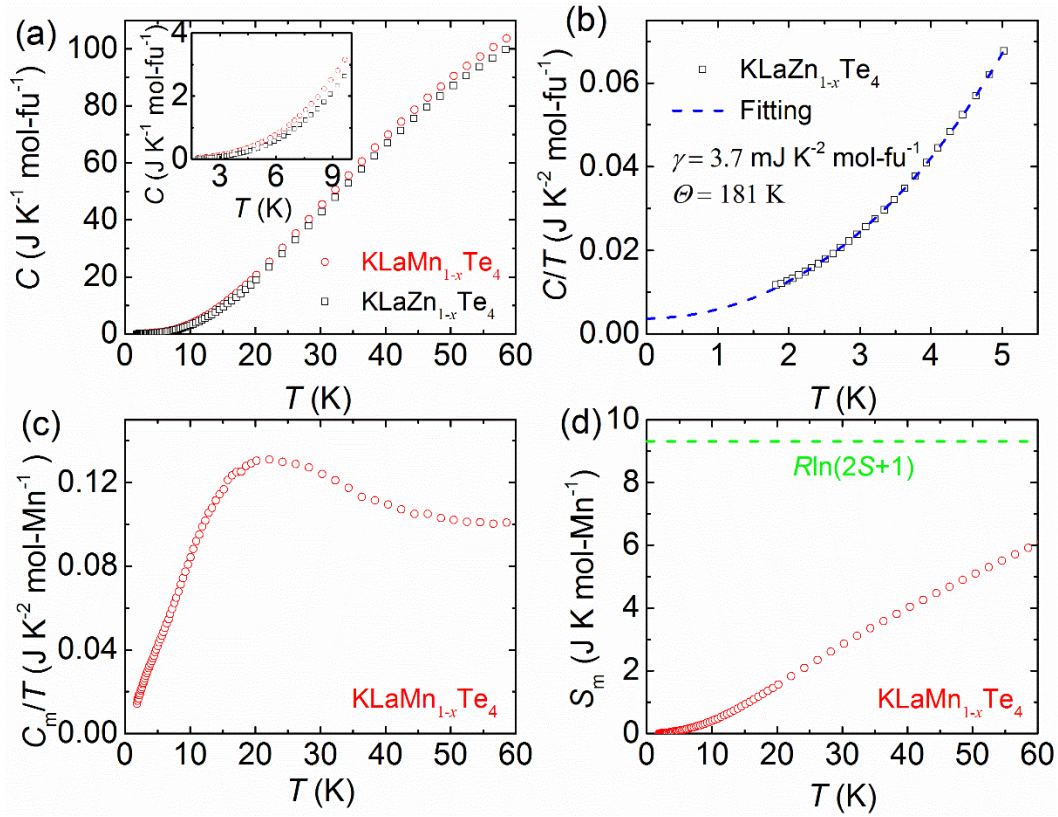


Figure 10. (a) Temperature-dependent specific heat C for $\text{KLaM}_{1-x}\text{Te}_4$ ($M = \text{Zn}, \text{Mn}$). Inset shows the data below 10 K. (b) Specific heat data fitting by considering phonon and electronic contribution for $\text{KLaZn}_{1-x}\text{Te}_4$. (c) Temperature dependence of magnetic contribution of specific heat over temperature C_m/T after subtracting phonon and electronic contribution in $\text{KLaMn}_{1-x}\text{Te}_4$. (d) Magnetic entropy S_m after integrating C_m/T curve in (c). The green dashed line corresponds to the value of total magnetic entropy loss of a spin-1 $R \ln(3)$.

For Table of Contents entry only

